

Research Article

Fractals and Independent Component Analysis for Defect Detection in Bridge Decks

Ikhlas Abdel-Qader,¹ Fadi Abu-Amara,² and Osama Abudayyeh³

¹Department of Electrical and Computer Engineering, Western Michigan University, Kalamazoo, MI 49008, USA

²Department of Computer Engineering, Al-Hussein Bin Talal University, Ma'an 71111, Jordan

³Department of Civil and Construction Engineering, Western Michigan University, Kalamazoo, MI 49008, USA

Correspondence should be addressed to Ikhlas Abdel-Qader, ikhlas.abdelqader@wmich.edu

Received 5 October 2010; Revised 24 April 2011; Accepted 14 June 2011

Academic Editor: John Mander

Copyright © 2011 Ikhlas Abdel-Qader et al. This is an open access article distributed under the Creative Commons Attribution License, which permits unrestricted use, distribution, and reproduction in any medium, provided the original work is properly cited.

We present in this paper a framework for the automatic detection and localization of defects inside bridge decks. Using Ground-Penetrating Radar (GPR) raw scans, this framework is composed of a feature extraction algorithm using fractals to detect defective regions and a deconvolution algorithm using banded-independent component analysis (ICA) to reduce overlapping between reflections and to estimate the radar waves travel time and depth of defects. Results indicate that the defects' estimated horizontal location and depth falling within 2 cm (76.92% accuracy) and 1 cm (84.62% accuracy) from their actual values.

1. Introduction

Ground-penetrating radar (GPR) is a nondestructive technique that creates a continuous two-dimensional cross-sectional image of the scanned medium and its internal objects. The GPR antenna transmits polarized pulses of electromagnetic waves through the scanned medium where portion of these radiations gets attenuated due to natural absorption. At the boundary between two electrically different materials (i.e., different dielectric constants or electrical conductivities), some radiations reflect back while the rest refract and continue their penetration. The A-scan and B-scan are the two commonly used formats for raw GPR data presentation. The A-scan, also known as a trace, is obtained by placing the GPR antenna above the target surface and recording reflected signals. The B-scan, also known as a line scan, is obtained by moving the GPR antenna over the target surface and recording the reflected signals at regular intervals. Each column of the B-scan is a single A-scan taken at a specific location.

According to a 2006 study by the American Society of Civil Engineers, 29% of bridges in the United States are considered structurally deficient or functionally obsolete due to overdue maintenance [1]. GPR can be used to detect

defects in concrete bridge decks [2, 3]. The most common defects in bridge decks are delaminations and air voids. Delaminations result from rebar corrosion due to moisture and deicing salts which causes a fracture plane to develop. This results in the creation of concrete-air-concrete interfaces in raw GPR scans. Figure 1 shows a simulated concrete bridge deck with embedded known defects (delaminations and voids).

Figure 2 is an example GPR scan of the simulated bridge deck. In this figure, three boundaries are shown: the air-surface of the concrete boundary resulting in the self-coupling bands, the concrete-rebar boundary resulting in the hyperbolic arcs, and the concrete-base boundary resulting in noncontinuous segments since reflections from targets under rebar peaks are masked by their strong reflections. Delaminations have a white-black-white reflection as shown in Figure 2. Air-filled voids have a black-white-black reflection due to the phase inversion since the electromagnetic waves propagate from a higher to a lower dielectric constant material (concrete-air interface).

The main challenge in using GPR for bridge deck condition assessment is the need for an experienced operator who can manually interpret raw scans and determine the defect types and locations. Since defects have irregular shapes

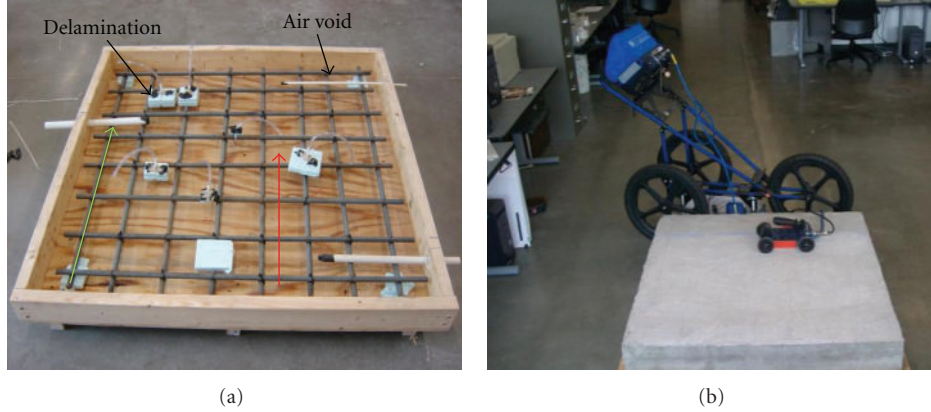


FIGURE 1: (a) is a simulated concrete bridge deck (slab) with embedded defects during construction. The green arrow indicates a parallel survey line to the first rebar from left (bottom rebar mesh) while the red arrow indicates a perpendicular survey line to the rebar (top rebar mesh). (b) is the finished slab.

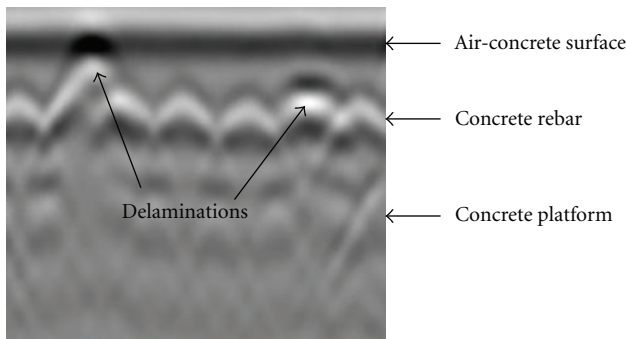


FIGURE 2: GPR scan data of a 6-inch concrete slab with two embedded delamination defects.

with different refractive indices from their surrounding medium, they emerge as new objects or layers in GPR scans. Consequently, automating the detection process will require a feature extraction method that can efficiently model different types of irregular shapes with reduced computational needs.

The reported work of using GPR in bridge deck condition assessment can be categorized into three groups: manual analysis, signal and image processing, and inverse scattering approaches. Manual analysis methods are time consuming, and the accuracy of the detection process depends on the technician's trained eye [2, 3]. The second group involves using signal and image processing methods to detect and/or characterize subsurface defects [4–8]. Unfortunately, none of the proposed methods were able to provide defect coordinates. Inverse scattering approaches use the Finite Difference Time Domain method as a subsurface modeling tool through approximating the physical geometry, material properties, and embedded targets [9]. Unfortunately, most of the developed models were not validated with real data from bridge decks to evaluate their performance in subsurface defects detection. Also, the developed models did not localize and characterize the subsurface defects.

This paper presents an automated algorithm for determining the coordinates of defects in bridge decks using only the underlying B-scan with no need for training the algorithm using other scans. Therefore, the proposed algorithm saves the time and effort involved in inspection and provides a more accurate condition assessment method.

2. Background

2.1. Fractal Analysis. The word *fractal* describes objects that are detailed at different scales. Most nature-made shapes such as defects in bridge decks are complex and have irregular edges. Therefore, a mathematical tool is needed to describe heterogeneity of real objects when classical Euclidean geometry fails to model.

Fractal sets can be divided into self-similar sets and self-affine sets. Self-similar sets describe data that repeat themselves (or their statistics) when different axes are magnified by the same factor while self-affine sets describe data that preserve their shape (or their statistics) only when different axes are scaled differently. Mathematically if a signal $x(t)$ has a fractal feature structure, then it should satisfy the scaling law under the scale conversion ($t \rightarrow \lambda t$)

$$X(\lambda t) = \lambda^H x(t), \quad (1)$$

where H is the Hurst exponent. If H is equal to 1, then $x(t)$ is a self-similar function otherwise it will be a self-affine function. For a signal, H will be in the range $[0, 1]$ as will be shown in (9).

Number of independent variables required to describe a point in a set is the topological dimension of that set. The Hausdorff-Besicovitch dimension (HBD) of a fractal set is a fractional number greater than its topological dimension that can be used to measure irregularity of that set. In practice, it is difficult to measure the HBD of a fractal set in its rigorous definition [10]. Therefore, several methods have been proposed in the literature to approximate it such as Fractal Brownian Motion (fBm), Box Counting Method (BCM), and Hurst Method (HM) [10]. Applying

these methods to the same set does not necessarily result in the same estimated value of fractal dimension (FD). These differences are due to the estimation algorithm used by a particular method which is application dependent. As a preprocessing stage, we compared between the performances of fBm, BCM, and HM and found fBm to be the most suitable for GPR data [11].

For a signal, the estimated fractal dimension will be in the range between 1 and 2. If the estimated FD is close to 1, a high neighbor-to-neighbor correlation will be present (smooth signal). If the estimated FD is close to 2, a high negative correlation will be present (nonsmooth signal). Figure 3 shows two traces extracted from the B-scan of Figure 2. The first one is extracted at the center of the defective region while the second one is extracted from its edge. Both traces have a topological dimension of 1, meaning that classical Euclidean geometry is unable to differentiate between them. On the other hand, both traces have different fractal dimensions with higher value for the first one. In other words, the estimated fractal dimension describes the relation between signal variance and the time scale.

Both roughness and topology of interfaces inside the scanned medium are imprinted in the recorded GPR traces where these traces are considered as self-affine functions of time [12]. A number of fractal-based algorithms were proposed in the literature to identify targets from raw GPR scans such as complex trace analysis [13] and fractal Brownian motion [14].

2.2. Deconvolution. A raw GPR trace (g) consists of a number of reflected pulses with each pulse being a delayed and attenuated version of the initial transmitted pulse (f). This can be modeled as a convolutive mixture of transmitted pulse (incident pulse) and impulse response of the scanned concrete slab (h) as shown in (2), resulting in one equation with two unknowns per reflected GPR trace:

$$g = f * h = \sum_j f(t_{i-j})h(t_j). \quad (2)$$

Such a problem can be solved using the deconvolution process to reduce overlapping between reflections from closely spaced targets and recover impulse response of the scanned slab. Many deconvolution algorithms have been proposed in the literature such as singular value decomposition (SVD) [15], subset selection deconvolution algorithm (SSDA) and banded-ICA [16, 17], maximum entropy blind deconvolution [18], and quasi-Newton blind deconvolution [19], to name a few.

Six different deconvolution methods including Wiener-based methods were examined in [7]. It was concluded that the Homomorphic deconvolution outperformed all the other techniques. Another comparison between different deconvolution approaches such as Wiener, Homomorphic, SVD, SSDA, and Discrete Wavelet transform for our GPR data is provided in [20]. It was concluded that SVD outperformed the other algorithms where the obtained measurements (amplitudes of the embedded targets and their depths) in the recovered impulse responses of the scanned

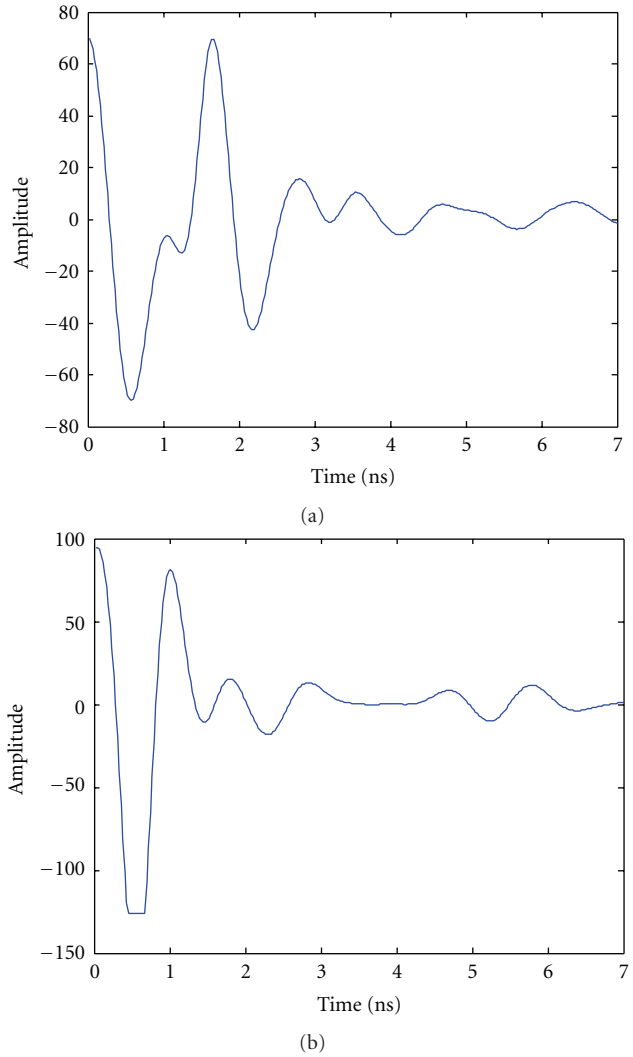


FIGURE 3: (a) and (b) are two scans extracted from B-scan of Figure 2 with fractal dimensions of 1.6 and 1.68, respectively. Both signals have a topological dimension of 1.

medium using SVD were closer to the actual measurements in comparison with results of the other algorithms.

The convolution process of (2) can be modeled using matrix operations ($g = Fh$) where the convolution matrix F is defined as

$$F_{n \times n} = \begin{bmatrix} f(t_1) & 0 & 0 & 0 & 0 & 0 \\ \vdots & f(t_1) & 0 & 0 & 0 & 0 \\ f(t_{nw}) & \vdots & \ddots & \vdots & \vdots & \vdots \\ 0 & f(t_{nw}) & f(t_1) & 0 & & \\ \vdots & 0 & \ddots & \vdots & & 0 \\ 0 & 0 & f(t_{nw}) & f(t_{nw-1}) & \cdots & f(t_1) \end{bmatrix}, \quad (3)$$

where nw is number of samples of the incident pulse vector $f = [f(t_1), f(t_2), \dots, f(t_{nw})]^T$, n is number of samples of the GPR trace g , t_i represents time index, and $i = 1, 2, \dots, nw$.

2.3. *ICA*. Independent component analysis is a statistical technique that can be used to decompose source signals $s_i(t)$ within observed signals $x_i(t)$. Equipped with (2) and by assuming the source signals have non-Gaussian distribution and statistically independent and identically distributed (i.i.d.) at different times, the linear ICA algorithm ($x = As$) can be used to model (2) where the GPR trace is defined as $x = [g(t_1), g(t_2), \dots, g(t_n)]^T$, its impulse response as $s = [h(t_1), h(t_2), \dots, h(t_n)]^T$, and the mixing matrix A is equal to the convolution matrix F ($A = F$). Statistically independent and identically distributed at different times signals description refer to the assumption that each signal has the same distribution as the other signals and all signals are mutually independent. Since an impulse response signal of the scanned concrete slab is a sparse signal representing the layered structure of that slab, it has a super-Gaussian distribution and thus it meets the non-Gaussianity requirement condition.

Utilizing the prior information about nature of the convolution matrix (i.e., banded matrix), the blind deconvolution problem can be converted into a blind source separation problem. However, this represents a single-input single-output ICA model which is inadequate for the underlying problem since statistics of the independent components cannot be characterized. In order to form a multidimensional ICA model ($X = AS$), time-delayed versions of $x(t)$ and $s(t)$ can be used to construct multidimensional matrices according to

$$\begin{aligned} X_{n \times n} &= [x(t-n+1)x(t-n+2) \cdots x(t-1)x(t)]^T, \\ S_{n \times n} &= [s(t-n+1)s(t-n+2) \cdots s(t-1)s(t)]^T. \end{aligned} \quad (4)$$

Unfortunately, these two equations are inadequate for the ICA model as is since the first few rows/columns of S and X have few nonzero elements meaning that statistics of the independent components cannot be constrained due to lack of information. To overcome this challenge, an approximate convolutional model is proposed to solve the lack of information problem by discarding the first few rows of X and S which consequently reduce the number of zero-valued elements in the first few rows [16, 17, 21]. Thus, (4) can be rewritten as

$$X_{m \times n} = [x(t-m+1)x(t-m+2) \cdots x(t-1)x(t)]^T, \quad (5)$$

$$S_{m \times n} = [s(t-m+1)s(t-m+2) \cdots s(t-1)s(t)]^T, \quad (6)$$

where size of the approximate convolution model (m) is less than size of the GPR trace (n). A number of ICA estimation methods have been reported in the literature such as Flexible ICA [22], Complex ICA [23], and Efficient FastICA (EFICA) which is a statistically efficient version of the FastICA algorithm with an added computational complexity [24]. However, it has superior separation performance as was reported in the literature [24, 25].

A number of banded-ICA deconvolution algorithms were proposed to deconvolve GPR traces [17, 26, 27]. As they reported, the estimated independent component is a delayed

version of the original source signal which prevents accurate depth estimation. Also, best value of m is determined manually for each case or assumed equal to the length of the corresponding GPR trace (n). The banded-ICA algorithm outperformed both the SVD and the SSDA algorithms in deconvolving GPR scans of simulated concrete bridge decks [16], however, the best value of m was determined manually for each trace which restricted the complete automation of defect detection process.

2.4. *Depth Estimation*. There are different methods to estimate depth of a target from GPR scans such as ground truth (velocity analysis), dielectric tables, and hyperbolic shape analysis [28]. Since the dielectric constant of concrete is in the range [4.5, 9], the dielectric tables' method assumes a dielectric constant value of 6.25 and approximates velocity of radar waves through the medium using (this equation is obtained from (8))

$$V = \frac{c}{\sqrt{\epsilon}}, \quad (7)$$

where c is speed of light in the vacuum (2.998×10^8 m/s) and ϵ is the dielectric constant. The depth of a defect is determined as

$$d_d = \frac{t_d c}{2\eta} = \frac{t_d c}{2\sqrt{\mu\epsilon}} \approx \frac{t_d c}{2\sqrt{\epsilon}} \approx \frac{t_d V}{2}, \quad (8)$$

where η represents refractive index of the target medium, ϵ represents the dielectric constant of the scanned medium, μ is its relative permeability, and t_d is the round-trip travel time between source and defect. In case of bridge decks, μ is approximately equal to one and thus $\eta \approx \sqrt{\epsilon}$. It is worthy to state here that the dielectric tables' method is the simplest but the least accurate method [28].

In the hyperbolic shape analysis method, the velocity of radar waves is estimated based on shape of the hyperbolic reflections using the Migration function in RADAN, a software package developed exclusively for GPR data by GSSI Inc. [29]. If the materials in the scanned medium have low dielectric constant, radar waves propagate with high velocity resulting in wide hyperbolae. This method does not require prior knowledge of a target's depth (such as rebar) to estimate the velocity, but requires a skillful operator to work with RADAN to manually analyze the GPR scans. Since the depth of rebar in bridge decks is known, the velocity analysis method will be used in this work to estimate depth of defects.

3. Defect Detection Framework and Modeling

The proposed framework consists of three stages to identify and localize defects in concrete as shown in Figure 4: a fractal analysis stage for the feature extraction, a banded-ICA stage for the deconvolution of the defective region traces, and a velocity analysis stage to estimate the depth of defects. As a preprocessing step, a zero correction is performed on raw B-scans that involves the deletion of first part of the B-scan all the way to the first positive peak of the ground band reflection. This step is intended to enable depth estimation with respect to the ground line.

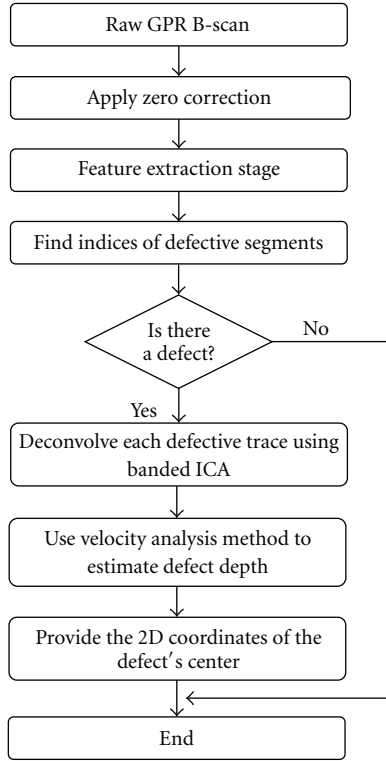


FIGURE 4: Block diagram of the proposed defect detection algorithm.

3.1. Fractal-Based Feature Extraction. In this work, a fractal-based feature extraction (FBFE) algorithm is proposed and applied to each A-scan extracted from the B-scan. FBFE can be summarized in the following steps after normalizing all traces to zero mean.

- (1) Feature vectors can be constructed according to the scanning method (see Figure 1(a)). In the case of having the survey line perpendicular to the rebar, the dominant reflections are from rebar and targets above it with the strongest reflections coming from the defect as shown in Figure 2. When the survey line is parallel to the rebar, most of the reflections are from deeper objects with rebar reflections being minimized as will be shown in Figure 13. These differences caused us to seek different feature vectors to characterize traces.

- (a) When the scan is conducted perpendicular to the rebar, the first feature vector, f_G , consists of time-domain statistical features such as fractal dimension (FD), root mean square (RMS), energy, and number of local maximum points (peaks). The RMS and energy are determined from the GPR trace and from its DFT real part values. The second feature vector, f_L , contains the value of the summation of peak-to-peak value at each local maximum point.
- (b) When the scan is parallel to the rebar, the first feature vector, f_G , is constructed in the same

way as in (a) above, but without the energy feature since it proved to be not efficient for defective and normal traces while the second vector feature, f_L , containing the square mean root (SMR) of each GPR trace which is viewed as a reasonable compromise between the geometric and the arithmetic means [30].

- (2) The fractal Brownian motion method is used to estimate the fractal dimension of the GPR trace $x(t)$ [17]. The double logarithmic plot of $E[x(t + \Delta t) - x(t)]^2$ versus step size, Δt , is obtained for various values of the step size Δt and the fractal dimension, FD, is estimated as

$$FD = 2 - H, \quad (9)$$

where $H \in [0, 1]$ is the Hurst exponent obtained from the slope of the linear segment of the fitted line between data points using the least squares method. Typically, H will be smaller for more irregular signals resulting in higher FD values. Since H is estimated from the linear segment, the error in H estimates will have minimal effect on the estimated FD value.

- (3) Each feature vector is a column in the feature matrices F_G and F_L .
- (4) The mean and standard deviation vectors, $(f_{G\mu}, f_{L\mu}, f_{G\sigma}, f_{L\sigma})$ are computed for all rows of the feature matrices F_G and F_L .
- (5) The index of segments of lengths greater than a threshold T , corresponding feature vectors in F_G that are greater than $f_{G\mu} + \alpha f_{G\sigma}$, and corresponding feature vectors in F_L matrix that are smaller than $f_{L\mu} + \alpha f_{L\sigma}$ where $\alpha \in [0, 1]$ are identified as defective regions.
- (6) The center trace within each defective segment is labeled as by the defect's column number. Dividing it over the total number of columns in the B-scan and multiplying it by the length of the B-scan, the horizontal location of defect is determined as

$$X_d = \frac{N_d}{N_c} \times L_s, \quad (10)$$

where N_d represents Defect's column number, N_c represents total number of columns in the B-scan (300–375 depending on the scan), and L_s represents length of the B-scan in cm.

A number of evaluation measures are used in this paper to assess the classification performance of the proposed FBFE algorithm. We define false negative FN as the case of failure to detect a defect and false positive FP as the case of declaring a nonexisting defect. Precision is defined according to (11) while recall is defined according to (12) as follows:

$$Pc = \frac{TP}{TP + FP}, \quad (11)$$

$$Rc = \frac{TP}{TP + FN}, \quad (12)$$

where TP represents number of correctly classified defects.

3.2. *Deconvolution Using Banded-ICA.* Our banded-ICA algorithm is a modified version of a previously developed algorithm in [16]. In the current version, we intended to increase sparseness of the estimated independent components so that they model the layered structure of the scanned medium. Also, the independent component with highest sparseness was selected as the best candidate while in the current version a more effective criterion is used to select the best candidate as will be shown in step (5). Finally, the size of the convolutional model m is determined automatically for each trace as explained in the parameter analysis, under the “size of the convolution model.” It can be summarized in the following steps.

- (1) Let x represent a defective trace marked by the FBFE algorithm.
- (2) The mixture matrix X is constructed according to (5).
- (3) Since the source signal to be estimated (impulse response) is sparse and consists a number of sharp spikes with relatively flat area between them (representing the layered structure of the scanned concrete deck), the separating matrix $W_{m \times m}$ is initialized to the identity matrix.
- (4) Mahalanobis transformation is used to whiten the mixture matrix X as follows:

$$Z = C^{-0.5}(X - \bar{X}), \quad (13)$$

where \bar{X} represents mean of the mixture matrix X and C represents its covariance matrix. The whitening step is a decorrelation process that results in an identity covariance matrix.

- (5) EFICA is used to decompose the whitened mixture matrix in order to recover m independent components. The selected independent component (best candidate) is to satisfy the following conditions.

- (a) It should have a minimum number of spikes n_s (since the defect may mask reflections from targets beneath it) as defined by

$$n_s = n_i - 1, \quad (14)$$

where n_i is the number of interfaces in the scanned concrete slab.

- (b) It should lead to the minimum mean square error (MMSE) according to

$$\text{MSE}_i = E(g - f * y_i)^2, \quad (15)$$

where g is the GPR trace and $*$ represents the convolution process between the estimated incident pulse of the GPR antenna f and the current estimated independent component or its horizontally flipped version, y_i , for all $i = 1, \dots, m$.

3.3. *Depth Estimation Using Velocity Analysis.* The velocity-analysis-based depth estimation method can be presented as follows.

- (1) The initial total range of a GPR trace is 10 ns. After applying zero-correction step, the new total range of the GPR trace is found using

$$T_n = \frac{L_z}{L_o} \times T_r, \quad (16)$$

where L_z represents the length of the trace after zero correction, L_o represents the original length of the trace, and T_r represents the total range.

- (2) Velocity of radar waves through layers of the scanned medium can be approximated using (17) (based on (8)) and noting that the depth of the rebar, d_r in the concrete bridge decks is known:

$$V = \frac{2d_r}{t_r}, \quad (17)$$

where V is the speed in cm/s, d_r is rebar depth in cm, and t_r is the round-trip travel time to the rebar.

- (3) Using (8), the actual depth of the defect is estimated. The spikes in the deconvolved trace are on a one-to-one correspondence with the ground line, defect, rebar, and bottom of the simulated deck as shown in Figure 8. The round-trip travel times of the rebar t_r and defect t_d are determined as

$$t_r = \frac{S_r}{L_{dt}} \times T_n, \quad t_d = \frac{S_d}{L_{dt}} \times T_n, \quad (18)$$

where S_r and S_d represent the corresponding spike location of the object (rebar or defect), L_{dt} represents the deconvolved trace length, and the new total range T_n was defined in (16).

4. Experimental Results

4.1. *Experimental Setup.* Two 15 cm deep concrete slabs were constructed to simulate bridge decks: one with several embedded defects of known dimensions and locations as shown in Figure 1 and one with no defects. PVC pipes and Styrofoam blocks were used to model air-void and delamination defects, respectively [2]. The slab is 114 cm long, 114 cm wide, and 15 cm deep with one bottom layer of rebar in both directions spaced at 15 cm on center and placed 6 cm and 7.5 cm deep with rebar cover of 6 cm. The simulated bridge decks are an accurate model of a single layer of rebar in reinforced concrete slabs where a single layer of rebar is a mesh of perpendicular steel bars embedded parallel to the concrete's surface at a single depth. While the rebar location in the concrete deck may vary from one bridge to another, it is known to the user from the bridge design documents (prior information). Additionally, the types and behavior of expected defects in bridge decks are also known. Therefore, simulating the defects is a reasonable approach in developing the algorithm using laboratory experiments.

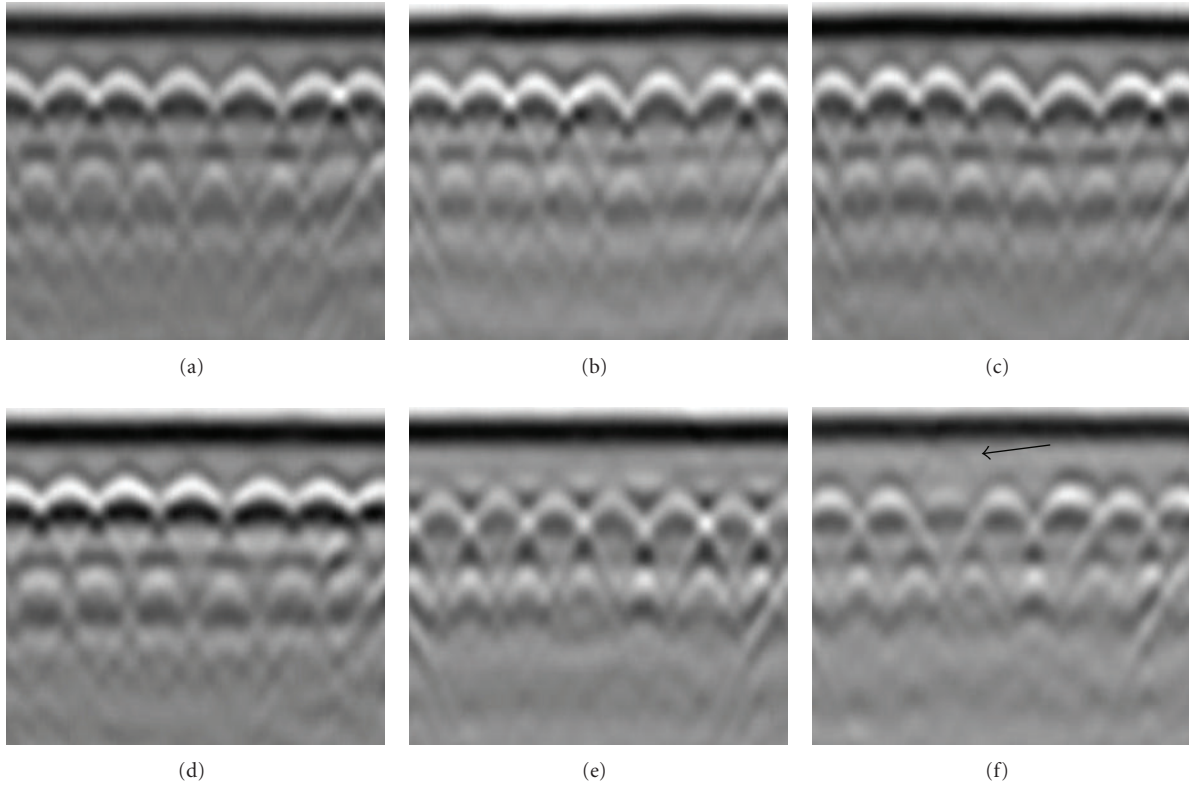


FIGURE 5: (a), (b), (c), (d), and (e) are five normal B-scans while (f) is a defective B-scan.

A 1.5 GHz (GSSI model 5100) bistatic antenna is used to scan the concrete slabs with the dielectric constant set to 6.25 [31]. Fourteen scans (labeled as scans 1 through 14) each of length 94 cm were collected of which five for the normal slab and nine for the defective one.

4.2. Results of the Defect Detection Algorithm. Figures 5(a), 5(b), 5(c), and 5(d) show normal scans (scan 1, scan 3, scan 4, and scan 8) with the survey line perpendicular to the rebar while Figure 5(e) (scan 12) shows a normal B-scan with the survey line parallel to the rebar.

Figure 5(f) (scan 13) shows a GPR scan data with embedded delamination defect that masked reflections from the third rebar. No defective segments are declared by the proposed fractal-based feature extraction algorithm after applying it to the aforementioned scans. The delamination defect in Figure 5(f) is barely visible with low contrast from its surrounding background. Therefore, the proposed FBFE algorithm was not able to detect this defect.

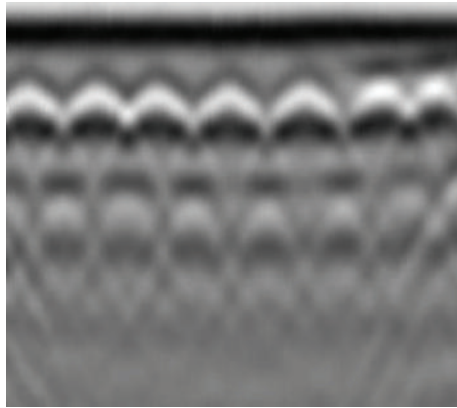
Table 1 shows results of applying the proposed FBFE algorithm to the nine defective scans. The proposed method detects eight of the nine defective scans. Further, the average difference between the estimated and actual horizontal location in the eight scans is 1.77 cm which indicates the applicability of the proposed algorithm in this field. Also, FBFE algorithm is able to detect and mark the defective regions using only the underlying B-scan with no need for the number of B-scans for algorithm training.

TABLE 1: Actual and estimated horizontal location of defects in the 15 cm slab*.

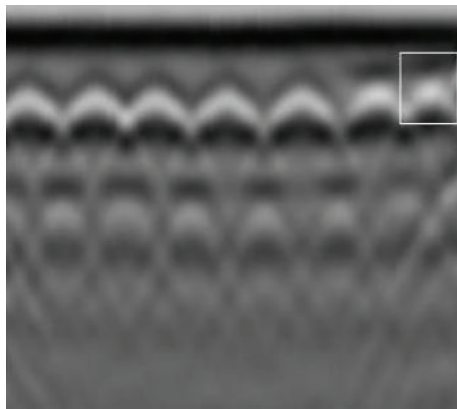
Scan	Actual location	Estimated location	Diff
Scan 2	85.73	87.07	1.34
Scan 5	22.23	22.12	0.11
	73.03	74.14	1.11
Scan 6	8.89	9.73	0.84
Scan 7	8.89	10.11	1.22
	16.51	17.15	0.64
Scan 9	27.31	24.46	2.85
Scan 10	8.26	6.96	1.30
	28.58	26.59	1.99
Scan 11	9.53	8.76	0.77
	48.26	44.73	3.53
Scan 13	36.83	ND	ND
Scan 14	49.53	54.89	5.36
	81.28	83.21	1.93
Average			1.77

* All measurements are in cm; ND means the defective segment is not detected.

Table 2 shows false positive, false negative, accuracy, precision, and recall for the FBFE algorithm applied the fourteen scans. As the table indicates, it has a zero false positive rate, low false negative rate, and high accuracy.



(a)



(b)

FIGURE 6: (a) and (b) are raw and processed B-scans with embedded air-void defect.

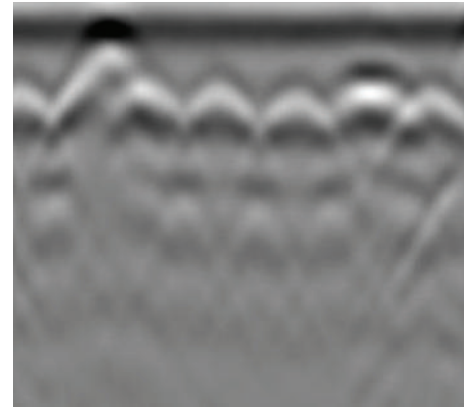
TABLE 2: False positive, false negative, accuracy, precision, and recall for the FBFE algorithm.

FP Rate	FN Rate	Accuracy	Precision	Recall
0%	4.76%	95.24%	100%	92.86%

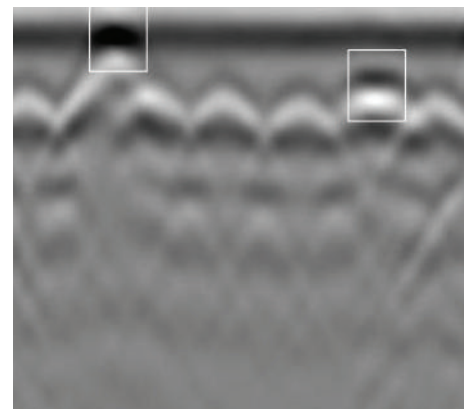
The fBm method takes the difference between a shifted version of the signal and the original signal which covers most of the neighbor-to-neighbor variations and consequently has high accuracy as Table 2 shows.

The marked defective traces from the FBFE method were used for the deconvolution process to reduce overlapping between reflections from adjacent targets and estimate the round-trip travel time to and from the embedded defects and rebar. The velocity analysis method is used to estimate depth (in cm) of detected defects as shown in Table 3. As the table shows, the estimated depth in all scans is within 1.3 cm from the actual depth. Also, the average difference between actual and estimated depth in all scans is 0.58 cm which shows robustness of the proposed method.

Given a raw B-scan as an input, applying the feature extraction algorithm followed by banded-ICA deconvolution algorithm marks the defective regions. Figure 6(a) shows raw B-scan (scan 2) with an embedded air-void defect that lies



(a)



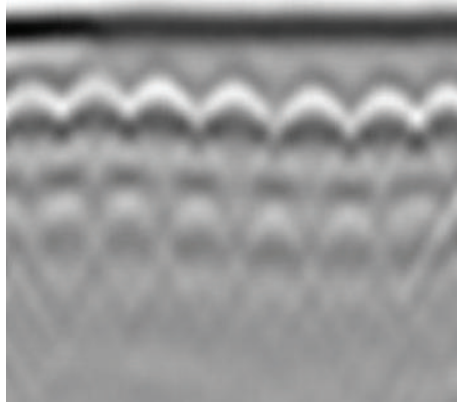
(b)

FIGURE 7: (a) and (b) are raw and processed B-scans with two embedded delamination defects.

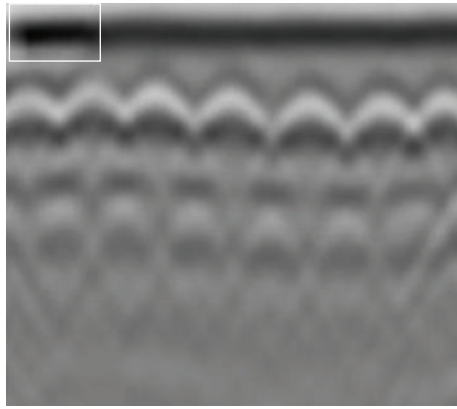
above the sixth and seventh hyperbolae. Figure 6(b) shows the processed scan where the defective region is partially marked. Figure 7(a) shows raw B-scan (scan 5) with two embedded delamination defects. The first defect is shallower than the other one and is partially overlapped with the black section of the ground coupling band, while the second defect lies right above the sixth hyperbola. Figure 7(b) shows the processed scan where the two defective regions are successfully marked.

Figure 8(a) shows a raw B-scan (scan 6) with a shallow embedded air-void defect that is overlapped with the black section of the ground coupling band. Figure 8(b) shows the processed scan where the defective region is successfully marked. Figure 9(a) shows raw B-scan (scan 7) with two embedded delamination defects that lie above the first and second hyperbolae where the first defect is shallower than the second one. Figure 9(b) shows the processed scan where the two defective regions are successfully marked.

Figure 10(a) shows a raw B-scan (scan 9) with shallow embedded air-void defect that is partially overlapped with the black section of the ground coupling band. Figure 10(b) shows the processed scan where the defective region is successfully marked. Figure 11(a) shows a raw B-scan (scan 10) with two embedded delamination and air-void defects.



(a)



(b)

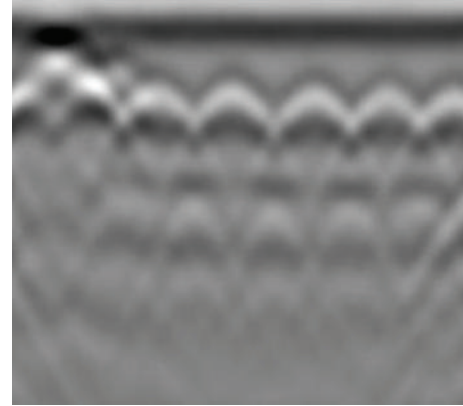
FIGURE 8: (a) and (b) are raw and processed B-scans with embedded air-void defect.

TABLE 3: Actual and estimated depth of defects in the 15 cm slab*.

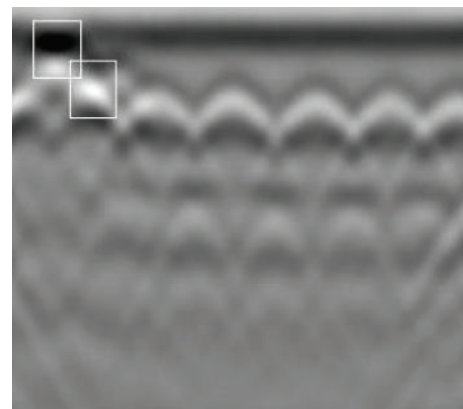
Scan	Actual depth	Estimated depth	Diff
Scan 2	3.61	4.78	1.17
Scan 5	2.54	2.98	0.44
	5.08	6.35	1.27
Scan 6	1	0.47	0.53
Scan 7	2.54	3.14	0.6
	3.81	4.41	0.6
Scan 9	1	1.53	0.53
Scan 10	2.54	1.95	0.59
	1	0.89	0.11
Scan 11	3.81	4.34	0.53
	2.54	2.41	0.13
Scan 13	5.08	ND	ND
Scan 14	5.08	4.13	0.95
	3.61	3.73	0.12
Average			0.58

*All measurements are in cm; ND means the defective segment is not detected.

The delamination defect has a low contrast and thus is barely visible while the air-void defect has a strong reflection



(a)



(b)

FIGURE 9: (a) and (b) are raw and processed B-scans with two embedded delaminations-defects.

and shallower than the delamination defect. Figure 11(b) shows the processed scan where both defects are successfully marked.

Figure 12(a) shows a raw B-scan (scan 11) with two embedded delaminations defects. Figure 12(b) shows the processed scan where the first and second defective regions are successfully and partially marked. Figure 13(a) shows a raw B-scan (scan 14) with two embedded delamination and air-void defects. Figure 13(b) shows the processed scan where both defects are partially marked.

None of the methods discussed in the literature were able to provide defect coordinates [4–8]. Our proposed framework localizes defects in bridge decks. This framework uses several parameters that impact the performance and accuracy of results such as dielectric constant value, minimum defective segment length, size of the convolutional model, and the parameter alpha. Our selection of these parameter values can be justified as follows.

Dielectric Constant ϵ . The dielectric constant reflects velocity of radar waves through the scanned medium. Higher value of the dielectric constant indicates a slower travel time and thus shallower penetration. The depth estimation accuracy depends on the proper choice of the dielectric constant

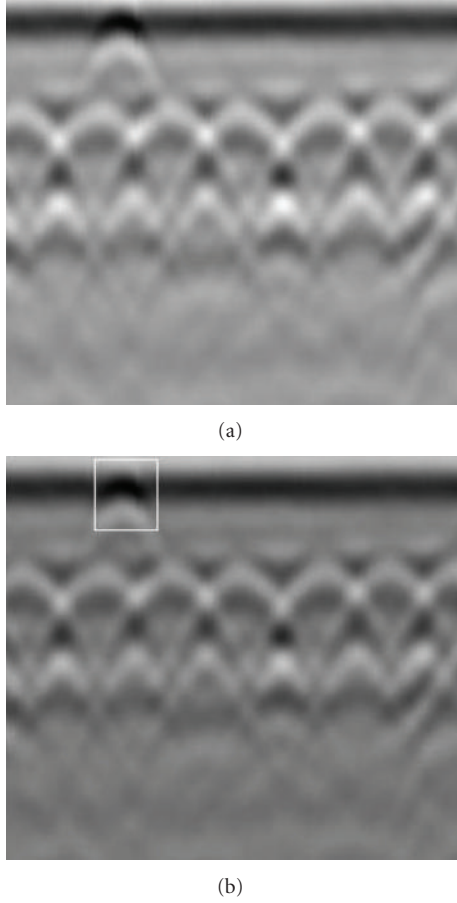


FIGURE 10: (a) and (b) are raw and processed B-scans with embedded air-void defect.

during the data collection process as (8) indicates. If the used value of the dielectric constant ϵ' during the data collection process is different from the proper value ϵ in the amount of Δ , then the estimated depth will be different from the actual depth as shown in

$$d' = \frac{ct}{2\sqrt{\epsilon'}} = \frac{ct}{2\sqrt{\epsilon \pm \Delta}}. \quad (19)$$

One possible way of finding the proper value of ϵ is by measuring velocity of radar waves through the scanned medium using the Migration function supplied by RADAN [29]. A hyperbola is fitted over a rebar hyperbola and, from which, speed of radar waves through the scanned medium is estimated (see the hyperbolic shape analysis method on page 5).

The estimated velocity of radar waves for the constructed slab is found as 12 cm/ns. Therefore, the dielectric constant is

$$\epsilon = \left(\frac{c}{v}\right)^2 = \left(\frac{3 \times 10^8 \times 100}{12 \times 10^9}\right)^2 = 6.25. \quad (20)$$

Since the concrete slab has homogenous materials, the dielectric constant should not change significantly with depth

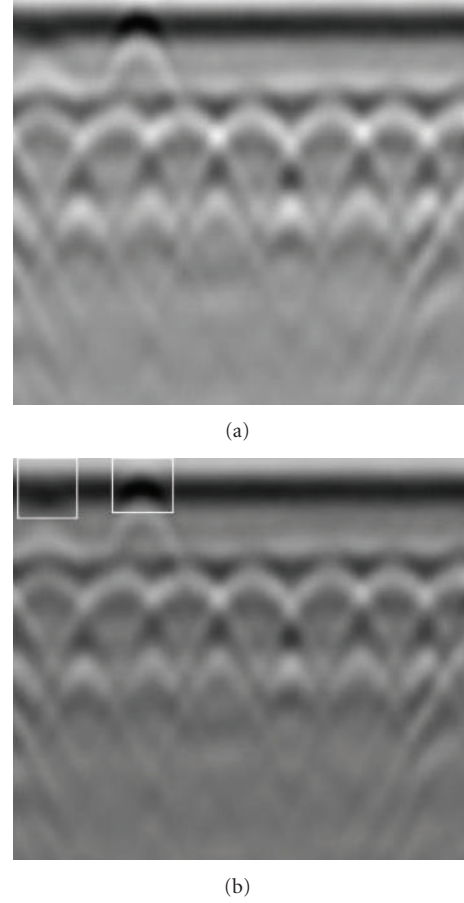


FIGURE 11: (a) and (b) are raw and processed B-scans with embedded delamination and air-void defects.

(as opposed to the soil). Therefore, assuming a constant value of the dielectric constant for the concrete slabs should not affect the depth estimation accuracy [31].

Minimum Defective Segment Length T. The densest recommended number of scans per cm for concrete structures using the 1.5 GHz antenna is 4 scans per cm [28]. The GPR antenna is set to 3.3 scans per cm during the data collection process. The determination of this number is based on the antenna frequency, estimated size of smallest target, and estimated depth of the shallowest target. The smallest defect embedded in the slabs is 3.81 cm wide. Ideally, T should be $3.3 * 3.81 = 12.5$ or less to detect the smallest defect expected. Since the proposed FBFE algorithm may detect parts of the defective region (see Figure 13) due to that fact that a defective region may have stronger reflections in some parts than other parts, the threshold value, T , is set to 7 to be able to detect defective regions as small as 2 cm. This user-defined parameter can be adjusted depending on the application nature.

Size of the Convolutional Model m. The variable m represents the number of independent components to recover during

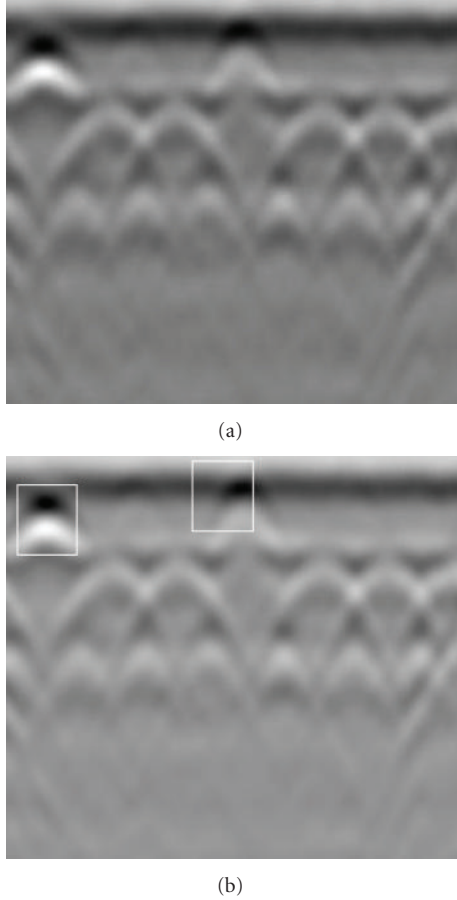


FIGURE 12: (a) and (b) are raw and processed B-scans with two embedded delamination defects.

the deconvolution step. Four defective traces were preprocessed to form a set of typical values of m according to $m = n - k$, where $k \in \{11, 32, 50, 54\}$ and n represents trace's length. For each new defective trace to be deconvolved, the value of m that minimized the mean square error (MMSE), according to (15), was chosen. The aim of the proposed algorithm is to qualify few numbers of traces (each one corresponds to a defective region center) to be deconvolved from the whole B-scan. Each defective trace models different objects at different depths. Therefore, using four typical values of m is more efficient than using a single value.

Parameter Alpha (α). The value of α is used to enable the algorithm in estimating the distance between the mean of features of traces within a region of interest and the mean of features of all traces in a B-scan. Figure 14(a) shows the distribution of the fractal dimension feature for scan 10 where the mean of all features in the B-scan is $\mu = 1.65$ and the standard deviation is $\sigma = 0.04$. Figure 14(b) shows the distribution of the RMS feature, where $\mu = 25.88$ and $\sigma = 2.56$, and Figure 14(c) shows the distribution of the energy feature, where $\mu = 676.2$ and $\sigma = 137.05$. Figure 14(d) shows the distribution of the number of local maximum points feature, where $\mu = 3.71$ and $\sigma = 0.52$. These

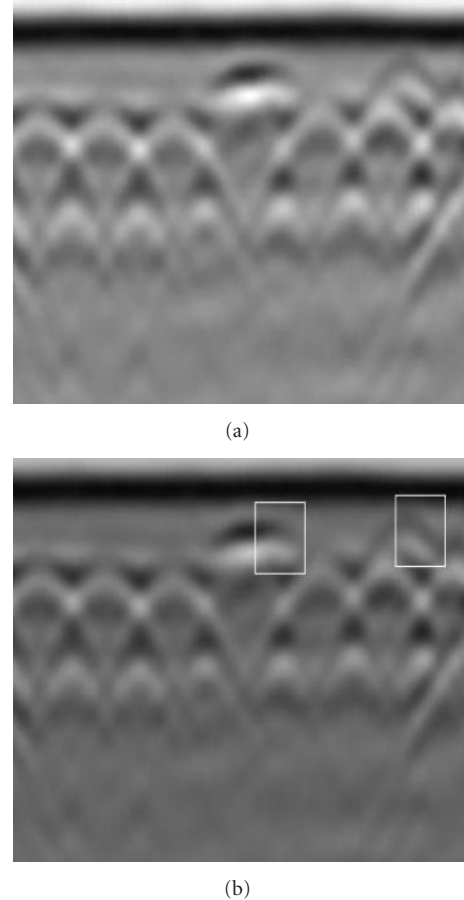


FIGURE 13: (a) and (b) are raw and processed B-scans with embedded delamination and air-void defects.

figures show that the statistical features used in the feature extraction algorithm are distributed over a small range around the mean, therefore, the mean is a good measure for the simulated bridge decks data. As we found from preprocessing, if α is within one distance from the standard deviation of the mean of all features in a B-scan, then this is sufficient to declare a region defective, resulting in $\alpha \in [0, 1]$. This allows the proposed algorithm to detect defective regions using only the underlying B-scan with no need for training the algorithm using other B-scans. Therefore, any value of α in the above range can be used. In this work, we chose $\alpha = 0.25$.

5. Concluding Remarks

An automated defect detection and localization framework for concrete bridge decks is presented in this paper. The framework consists of three algorithms: (1) fractal-based feature extraction algorithm to detect defective regions; (2) banded-ICA deconvolution algorithm to reduce overlapping reflections from closely spaced targets and to recover travel time to and from detected defects and rebar; (3) velocity analysis method to estimate depth of detected defects. This framework was implemented and tested using fourteen raw

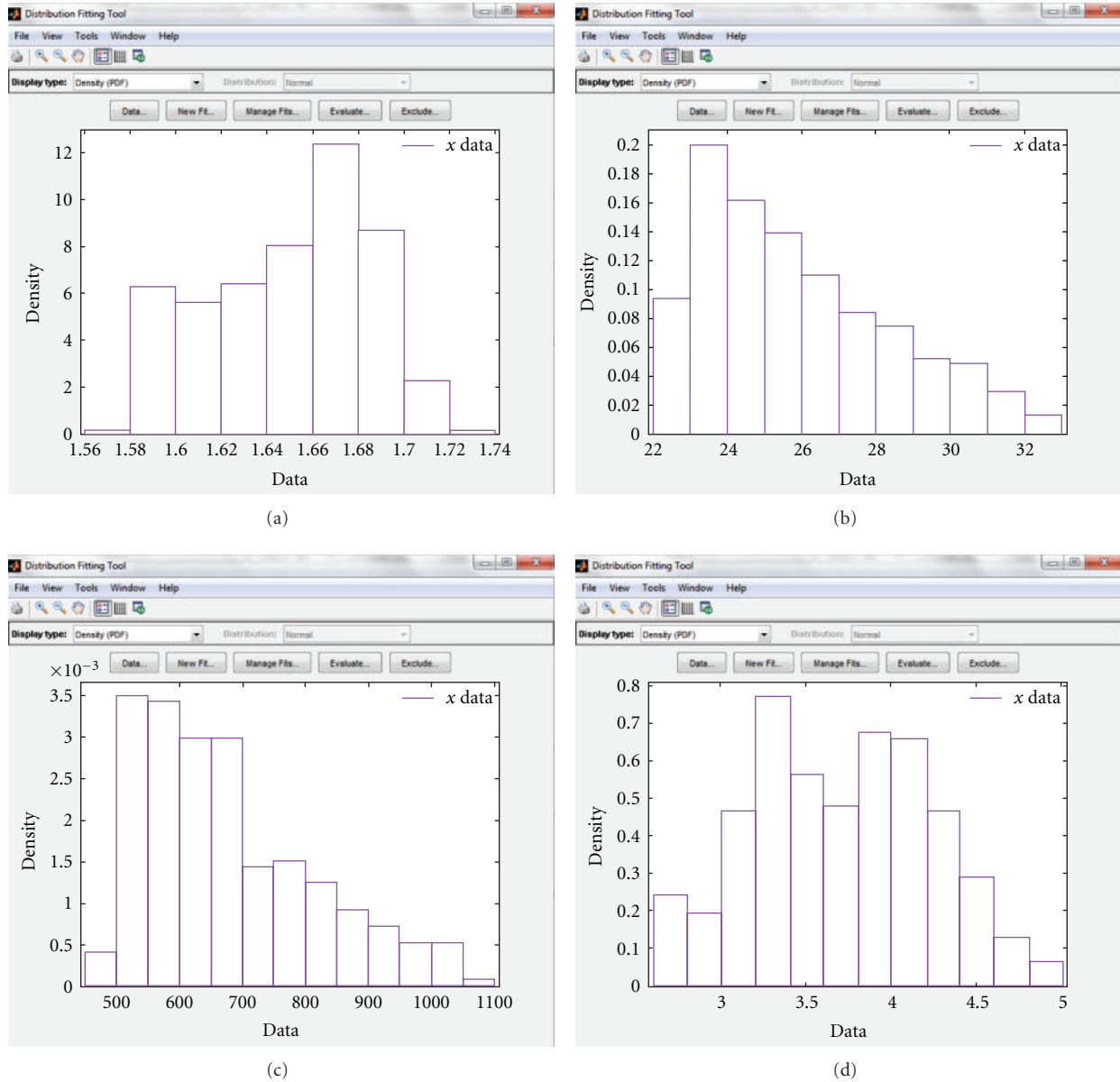


FIGURE 14: Distribution of the statistical features (fractal dimension, RMS, energy, and number of local maximum points) used for scan 10.

GPR scans of two simulated 15 cm concrete bridge decks with known defect types and locations; five of the fourteen are from the normal slab, and the rest are from the defective one. The nine defective scans contained fourteen defective regions.

At the boundary (e.g., change of material, moisture) between two electrically different materials (i.e., different dielectric constants or electrical conductivities), some of the transmitted GPR radiations reflect back while the rest refract and continue their penetration. The reflected radiations at the boundaries appear as spikes in the impulse response of the scanned medium, making the detection of these layers (and potentially defects) possible.

Results indicate that the FBFE algorithm detected thirteen out of fourteen defective regions with average difference

between actual and estimated horizontal locations of 1.77 cm resulting in high accuracy, recall, and precision. Results also demonstrate that the FBFE algorithm has low false negative and false positive rates. The proposed FBFE algorithm is able to detect and mark defective regions using only the underlying B-scan with no need for a number of B-scans for the purpose of algorithm training as required by other methods. Additionally, the results of the banded-ICA deconvolution algorithm and the velocity analysis method indicate that the average difference between actual and estimated depth is 0.58 cm.

Finally, the current state of the art in GPR-based condition assessment is focused on identification (full or partial) of defective regions without localization. Our integrated FBFE and banded-ICA framework was also able to correctly

identify and label the defective regions (thirteen out of fourteen—nine full and four partial). In addition, we were able to fully identify defect coordinates for nine cases and to partially mark four additional cases. Since our ultimate goal is to maximize full defect detection, future work will focus on further refinements to the algorithm to improve the full detection results.

While the banded-ICA deconvolution algorithm is robust, it is computationally demanding. Therefore, future work should improve its execution time and reduce its computational complexity. Future work should also focus on integrating a classifier into our framework for defect-type characterization. Finally, future work will focus on evaluating and validating the proposed framework using real bridges' GPR data.

Acknowledgments

Partial support of this work was provided by Western Michigan University FRACAA-2009 Award. The authors would like to acknowledge Western Michigan University for its support and contributions to the Information Technology and Image Analysis (ITIA) Center.

References

- [1] B. Cross, "2006 structural engineering and public safety," in *Proceedings of the 2006 Structures Congress*, pp. 18–21, May 2006.
- [2] S. Nabulsi, O. Abudayyeh, S. Yehia, and I. Abdel-Qader, "The detection of common concrete bridge deck defects using thermography, impact echo, and ground penetrating radar," Tech. Rep. CEM-05-01, Department of Civil and Construction Engineering, Western Michigan University, Kalamazoo, Mich, USA, 2005.
- [3] O. Abudayyeh, S. Yehia, A. Zalt, and I. Abdel-Qader, "GPR imaging for bridge deck condition assessment," *Bridge Structure Taylor and Francis*, vol. 4, no. 2, pp. 75–86, 2008.
- [4] H. Liu, "An efficient concrete bridge disease identification system based on sample database," in *Proceedings of the International Symposium on Computer Science and Computational Technology, (ISCST '08)*, pp. 184–188, December 2008.
- [5] T. C. Hutchinson and Z. Chen, "Image-based framework for concrete surface crack monitoring and quantification," *Advances in Civil Engineering*, vol. 2010, Article ID 215295, 18 pages, 2010.
- [6] M. M. Reda Taha, "A neural-wavelet technique for damage identification in the ASCE benchmark structure using phase II experimental data," *Advances in Civil Engineering*, vol. 2010, Article ID 675927, 13 pages, 2010.
- [7] S. Lahouar, *Development of data analysis algorithms for interpretation of ground penetrating radar data*, Dissertation, Virginia Polytechnic Institute and State University, Blacksburg, Va, USA, 2003.
- [8] H. J. Shin, *Probabilistic bridge deck condition analysis using ground penetrating radar (GPR)*, Dissertation, Rensselaer Polytechnic Institute, Troy, NY, USA, 2004.
- [9] K. M. Belli, *Ground penetrating radar bridge deck investigations using computational modeling*, Dissertation, The Department of Mechanical and Industrial Engineering, Northeastern University, Boston, Mass, USA, 2008.
- [10] K. Falconer, *Fractal Geometry Mathematical Foundations and Applications*, Wiley, West Sussex, UK, 2nd edition, 2003.
- [11] F. Abu-Amara and I. Abdel-Qader, *An automated framework for defect detection in concrete bridge decks using fractals and independent component analysis*, Dissertation, Western Michigan University, Kalamazoo, Mich, USA, 2010.
- [12] K. Oleschko, G. Korvin, A. S. Balankin et al., "Fractal scattering of microwaves from soils," *Physical Review Letters*, vol. 89, no. 18, 2002.
- [13] S. K. Nath and P. Dewangan, "Detection of seismic reflections from seismic attributes through fractal analysis," *Geophysical Prospecting*, vol. 50, no. 3, pp. 341–360, 2002.
- [14] Y. Zhao, J. Wu, M. Wan, and X. Xie, "Fractal technique for abstracting high-resolution information from GPR section," in *Proceedings of the 10th International Conference Ground Penetrating Radar (GPR '04)*, pp. 21–24, June 2004.
- [15] I. Markovsky and S. van Huffel, "Overview of total least-squares methods," *Signal Processing*, vol. 87, no. 10, pp. 2283–2302, 2007.
- [16] I. Abdel-Qader, O. Abudayyeh, V. Krause, and F. Abu-Amara, "Comparative study of deconvolution algorithms applied to GPR images of concrete bridge decks," Tech. Rep. ITIA-2010-01, Information Technology and Image Analysis Center, College of Engineering and Applied Sciences, Western Michigan University, 2010.
- [17] S. T. Kaplan and T. J. Ulrych, "Blind deconvolution and ICA with a banded mixing matrix," in *Proceedings of the 4th International Conference on Independent Component Analysis and Blind Signal Separation (ICA '03)*, pp. 591–596, Nara, Japan, April 2003.
- [18] M. Pinchas and B. Z. Bobrovsky, "A Maximum Entropy approach for blind deconvolution," *Signal Processing*, vol. 86, no. 10, pp. 2913–2931, 2006.
- [19] D. T. Pham, "Generalized mutual information approach to multichannel blind deconvolution," *Signal Processing*, vol. 87, no. 9, pp. 2045–2060, 2007.
- [20] A. Koirala and I. Abdel-Qader, "Investigation of deconvolution methods for bridge decks GPR signals," Tech. Rep. 2007-101, The Information Technology and Image Analysis (ITIA) Center, Western Michigan University, 2007.
- [21] A. Hyvarinen, J. Karhunen, and E. Oja, *Independent Component Analysis*, John Wiley & Sons, New York, NY, USA, 2001.
- [22] K. Kokkinakis and A. K. Nandi, "Generalized gamma density-based score functions for fast and flexible ICA," *Signal Processing*, vol. 87, no. 5, pp. 1156–1162, 2007.
- [23] S. C. Douglas, "Fixed-point algorithms for the blind separation of arbitrary complex-valued non-Gaussian signal mixtures," *Eurasip Journal on Advances in Signal Processing*, vol. 2007, Article ID 36525, 15 pages, 2007.
- [24] Z. Koldovský, P. Tichavský, and E. Oja, "Efficient variant of algorithm FastICA for independent component analysis attaining the Cramér-Rao lower bound," *IEEE Transactions on Neural Networks*, vol. 17, no. 5, pp. 1265–1277, 2006.
- [25] P. Tichavsky, Z. Koldovsky, A. Yeredor, G. Gomez-Herrero, and E. Doron, "A hybrid technique for blind separation of non-Gaussian and time-correlated sources using a multicomponent approach," *IEEE Transactions on Neural Networks*, vol. 19, no. 3, pp. 421–430, 2008.
- [26] C. L. Bastard, V. Baltazart, Y. Wang, and J. Saillard, "Thin-pavement thickness estimation using GPR with high-resolution and superresolution methods," *IEEE Transactions on Geoscience and Remote Sensing*, vol. 45, no. 8, pp. 2511–2519, 2007.

- [27] A. Al-Qaisi, W. L. Woo, and S. S. Dlay, "Novel statistical approach to blind recovery of earth signal and source wavelet using independent component analysis," *WSEAS Transactions on Signal Processing*, vol. 4, no. 4, pp. 231–240, 2008.
- [28] *GSSI Handbook for Radar Inspection of Concrete*, Geophysical Survey Systems, Inc., Salem, NH, USA, 2006.
- [29] The Geophysical Survey Systems, Inc., 2011, <http://www.geophysical.com/software.htm>.
- [30] D. B. Stephenson, K. Rupa Kumar, F. J. Doblus-Reyes, J. F. Royer, F. Chauvin, and S. Pezzulli, "Extreme daily rainfall events and their impact on ensemble forecasts of the Indian monsoon," *Monthly Weather Review*, vol. 127, no. 9, pp. 1954–1966, 1999.
- [31] *TerraSIRch SIR System-3000 User's Manual*, Geophysical Survey Systems, Inc., Salem, NH, USA, 2004.



Hindawi

Submit your manuscripts at
<http://www.hindawi.com>

